On the Relation between Thermohaline Anomalies and Water Mass Transformation in the Eastern Subpolar North Atlantic

LEILANE PASSOS,[a,b,c,d] HELENE R. LANGEHAUG,[b,c] MARIUS ÅRTHUN,[a,b] AND FIAMMETTA STRANEO[e]

[a] *University of Bergen, Bergen, Norway*
[b] *Bjerknes Centre for Climate Research, Bergen, Norway*
[c] *Nansen Environmental and Remote Sensing Center, Bergen, Norway*
[d] *College of Earth, Ocean, and Atmospheric Sciences, Oregon State University, Corvallis, Oregon*
[e] *Scripps Institution of Oceanography, University of California San Diego, La Jolla, California*

(Manuscript received 10 July 2023, in final form 26 April 2024, accepted 24 May 2024)

ABSTRACT: Decadal thermohaline anomalies carried northward by the North Atlantic Current are an important source of predictability in the North Atlantic region. Here, we investigate whether these thermohaline anomalies influence surface-forced water mass transformation (SFWMT) in the eastern subpolar gyre using the reanalyses EN4.2.2 for the ocean and the ERA5 for the atmosphere. In addition, we follow the propagation of thermohaline anomalies along two paths: in the subpolar North Atlantic and the Norwegian Sea. We use observation-based datasets (HadISST, EN4.2.2, and Ishii) between 1947 and 2021 and apply complex empirical orthogonal functions. Our results show that when a warm anomaly enters the eastern subpolar gyre, more SFWMT occurs in light-density classes (27.0–27.2 kg m^{-3}). In contrast, when a cold anomaly enters the eastern subpolar gyre, more SFWMT occurs in denser classes (27.4–27.5 kg m^{-3}). Following the thermohaline anomalies in both paths, we find alternating warm–salty and cold–fresh subsurface anomalies, repeating throughout the 74-yr-long record with four warm–salty and cold–fresh periods after the 1950s. The cold–fresh anomaly periods happen simultaneously with the Great Salinity Anomaly events. Moreover, the propagation of thermohaline anomalies is faster in the subpolar North Atlantic (SPNA) than in the Norwegian Sea, especially for temperature anomalies. These findings might have implications for our understanding of the decadal variability of the lower limb of the Atlantic meridional overturning circulation and predictability in the North Atlantic region.

SIGNIFICANCE STATEMENT: Anomalously warm–salty or cold–fresh water, carried by the North Atlantic Current toward the Arctic, is a source of climate predictability. In this study, we investigate 1) how these ocean anomalies influence the transformation of water masses in the eastern subpolar gyre and 2) their subsequent propagation poleward and northwestward. The key findings reveal that anomalously warm waters entering the eastern subpolar gyre lead to increased transformation in lighter water masses, while cold anomalies affect denser water masses. These anomalies propagate more than 2 times faster toward the Greenland coast (northwestward) than toward the Arctic (poleward). Our findings contribute to enhancing the understanding of decadal predictability in the northern North Atlantic, including its influence on the Atlantic meridional overturning circulation.

KEYWORDS: North Atlantic Ocean; Meridional overturning circulation; Thermohaline circulation; Water masses/storage; Decadal variability; Oceanic variability

1. Introduction

The Atlantic meridional overturning circulation (AMOC) in the subpolar North Atlantic Ocean involves the transformation of warm surface waters, in the northward-flowing North Atlantic Current (NAC), into cold and dense waters transported southward (Lozier et al. 2019; Petit et al. 2020). Recent studies have demonstrated that a large part of this transformation takes place in the eastern subpolar gyre (east of 30°W) by local buoyancy forcing (Lozier et al. 2019; Li et al. 2021; Koman et al. 2022). Variations in the buoyancy-driven water mass transformation can be a result of both variable air–sea fluxes and changes in the surface density field. For the eastern subpolar gyre, Petit et al. (2021) showed that surface density rather than buoyancy fluxes influences changes in the transformation of Subpolar Mode Water. However, others highlight the role of buoyancy fluxes (Petit et al. 2020; Grist et al. 2016; Lozier et al. 2017).

In the eastern subpolar gyre, the temperature and salinity variability on decadal time scales is associated with the propagation of anomalies along the NAC (Holliday et al. 2008; Årthun et al. 2017). Several studies suggest that a combination of ocean advection and the local atmosphere–ocean interaction governs the propagation of anomalous temperature (e.g., Saravanan and Mcwilliams 1998; Krahmann et al. 2001).

Denotes content that is immediately available upon publication as open access.

Supplemental information related to this paper is available at the Journals Online website: https://doi.org/10.1175/JCLI-D-23-0379.s1.

Corresponding author: Leilane Passos, leilane.passos@oregonstate.edu

DOI: 10.1175/JCLI-D-23-0379.1

However, recent studies have pointed out ocean advection as the main mechanism driving decadal changes in ocean heat content and temperature variability of water masses within the eastern subpolar gyre (de Boisséson et al. 2012; Desbruyères et al. 2015).

Variations in water mass transformation influence AMOC's lower limb on interannual to decadal time scales (Marsh 2000). Recently, Desbruyères et al. (2019) highlighted the role of water mass transformation in high latitudes as a surface predictor for AMOC's lower limb variability, with a 5–6-yr time lag. While previous literature suggests a connection between the surface-forced water mass transformation (SFWMT) and thermohaline (temperature and salinity) anomalies carried by currents in the eastern subpolar gyre (Thierry et al. 2008), a clear understanding of this link is still lacking. Thus, the primary focus of this paper is to investigate the extent to which decadal thermohaline anomalies are reflected in the SFWMT within the eastern subpolar North Atlantic.

The thermohaline anomalies carried by the NAC can follow two main routes after crossing the eastern subpolar region (Fig. 1): 1) following a northwestward branch in the subpolar North Atlantic, going all the way to the Labrador Sea (Daniault et al. 2016); and 2) following a northward branch, crossing the Iceland–Scotland Ridge, reaching the Norwegian Sea and later the Barents Sea and the Fram Strait.

The thermohaline anomalies that cross the Iceland–Scotland Ridge impact Arctic sea ice (Yeager et al. 2015; Årthun et al. 2012) and marine ecosystems (Fossheim et al. 2015; Fransner et al. 2023) and have been suggested as a main source of climate predictability in the Norwegian Sea and the Barents Sea on the decadal time scale (Onarheim et al. 2015; Årthun et al. 2017). On the other hand, the propagation of anomalous heat and salt that follows the northwestward branch holds implications for the climate variability on the south coast of Greenland and the Labrador Sea (Belkin et al. 1998; Belkin 2004). Along the two pathways, there are likely differences in air–sea interaction and mixing with other water masses, which may result in different evolution of the thermohaline anomalies. Therefore, the secondary focus of this paper is to compare the differences and similarities in the propagation of thermohaline anomalies along these two pathways after their advection through the eastern subpolar gyre.

Decadal variability in North Atlantic sea surface temperatures has been associated with predictable fluctuations in the climate over western Europe and North America (Collins and Sinha 2003; Jacob et al. 2005; Yin and Zhao 2021). A better understanding of thermohaline anomalies in the North Atlantic Ocean and its along-path modification could, therefore, benefit society through the improvement of long-term forecasts (Merryfield et al. 2020; Payne et al. 2022). Furthermore, this investigation offers potential observational benchmarks for guiding improvements in prediction systems within the North Atlantic region.

The paper is structured as follows. Section 2 presents the observation-based datasets and the methodology used to compute SFWMT and the complex empirical orthogonal functions (CEOFs). Section 3 gathers the main results of the study, and sections 4 and 5 discuss and summarize them, respectively.

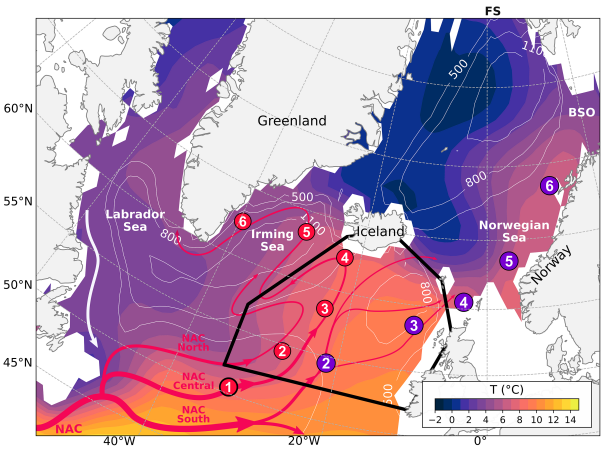

FIG. 1. Mean subsurface temperature at 315 m for the North Atlantic–Arctic region highlighting the SPNA-pathway (red circles) and the NS-pathway (purple circles). Throughout the document, stations from the SPNA-pathway are denoted as SPNA-st1 until SPNA-st6, while stations from the NS-pathway are referred to as NS-st1 until NS-st6. The black polygon defines the eastern subpolar gyre. The continuous white lines are the isolines of 500, 800, and 1100 m of the mean winter mixed layer depth for 1947–2021. The results are from EN4.2.2. The pink arrows, together with the white arrow, represent the circulation of the SPNA gyre, where NAC is the North Atlantic Current and its south, central, and north branches. BSO is the Barent Sea Opening, while the FS outside the map is the Fram Strait.

2. Data and methods

a. Observation-based datasets

To evaluate the variability of temperature and salinity in the North Atlantic, we mainly use the objective analyses of Met Office quality-controlled ocean temperature and salinity (Good et al. 2013) version EN4.2.2. In addition to EN4.2.2, we also utilize other datasets to assess the sensitivity of our results. These include the Met Office Hadley Centre Sea Ice and Sea Surface Temperature dataset, version 1.1 (HadISST1.1) (Rayner et al. 2003), and the Ishii Ocean Analyses Project dataset (Ishii et al. 2005). While slight variations exist among the datasets, our overall findings remain consistent and are not significantly affected by these differences. All datasets are available in a regular grid with a spatial resolution of 1° × 1° and monthly temporal resolution. Please refer to Table 1 for more detailed information.

The analysis focuses on the boreal winter due to the most vigorous atmosphere–ocean coupling during this period when SST variability reflects upper-ocean heat content variability as SST anomalies reach the base of the deep winter mixed layer (Alexander and Deser 1995; Watanabe and Kimoto 2000). Winter is defined here as January–April. To evaluate the variability of hydrographic anomalies (temperature and salinity), we defined stations following the pathway of the Atlantic Water within the subpolar North Atlantic (SPNA) and Norwegian Sea (NS) (red and purple circles, respectively, Fig. 1). To define the stations in the NS-pathway, we referred to previous studies by Årthun et al. (2017) and Langehaug et al. (2018).

TABLE 1. Observation-based datasets used to evaluate the variability of temperature and salinity anomalies in the North Atlantic. WOD: World Ocean Database. ASBO: Arctic Synoptic Basinwide Oceanography. GTSPP: Global Temperature and Salinity Profile Programme. COBE: Centennial in situ Observation-Based Estimates of the variability of SST and marine meteorological variables. The reference period for anomaly calculations considers the "Period analyzed" column for each dataset.

	Period analyzed	Data assimilated
HadISST	1947–2021	Met Office Marine, Data Bank, and satellite data
EN4.2.2	1947–2021	WOD18, GTSPP, Argo, and ASBO
Ishii	1947–2012	WOD01, GTSPP, Argo, IRD, and COBE

While the stations in the SPNA-pathway do not precisely align with the anticyclonic gyre in the subpolar North Atlantic, this deviation does not affect our results. To define the stations in this pathway, we aimed to follow the position of the boundary current in the area, by selecting stations within the 1000–2000-m depth range. We kept an equivalent number of stations to those along the NS-pathway for consistency. Analyzes for both pathways were performed at the surface and subsurface (~300 m) for all datasets.

We analyzed the monthly uncertainties provided by the EN4.2.2 product for each station within both pathways (Figs. 1a,b in the online supplemental material). In the NS-pathway, errors do not change considerably over time in four out of six stations for both temperature and salinity (the amplitude of the error depends on the station). However, across the SPNA-pathway, errors display more variability, particularly preceding the Argo era, consistent with Biló et al. (2022) analysis, which found significant monthly salinity uncertainties prior to this period in EN4.2.2. Moreover, Jones et al. (2023) found excellent agreement between Argo gridded profiles and EN4 grid cells in depths <2000 m.

In the Norwegian Sea, a comparison between EN4.2.2, Ishii, HadISST, and direct surface temperature observations from station M (Hughes et al. 2009) showed similar decadal variability across all datasets and observations (supplemental Fig. 2). In the subpolar North Atlantic, Biló et al. (2022) demonstrated that EN4.2.2 exhibits interannual-to-decadal variability consistent with Global Ocean Reanalysis and Simulation (GLORYS), Advance Radar for Meteorological and Operational Research (ARMOR3D), and the Roemmich–Gilson (RG) Argo floats' climatology. Notably, both EN4.2.2 and Ishii display similar winter variability in temperature and salinity across stations in both pathways (supplemental Figs. 1a,b). Considering this, we hold confidence in utilizing EN4.2.2 for our decadal analyses in both pathways.

b. *Surface-forced water mass transformation*

The SFWMT will be quantified according to the method developed by Walin (1982) and Speer and Tziperman (1992), which show that the SFWMT in an outcrop region due to surface fluxes is equivalent to the volume transport across the outcropping isopycnal in an ocean at rest. Other processes like mixing and entrainment contribute to the water mass transformation. However, in the subpolar North Atlantic, the surface fluxes play the main role in water mass transformation (Marsh 2000; Desbruyères et al. 2019). The SFWMT is calculated monthly for each grid point based on the surface buoyancy flux according to Eq. (1) (Speer and Tziperman 1992).

$$\mathrm{SFWMT}(\sigma^*) = \frac{1}{\Delta\sigma}\int\int\left[-\frac{\alpha}{C_P}Q_H + \beta\frac{S}{1-S}Q_S\right]\Pi(\sigma)dxdy, \tag{1}$$

where C_P is the specific heat capacity of water (3996 J kg^{-1} K^{-1}); α and β are the thermal expansion coefficient and haline contraction coefficient, respectively, calculated varying in time and space; and S is the nondimensional surface salinity. We estimated all parameters and potential density using the Gibbs Seawater Oceanographic Toolbox 3.06.12 software (McDougall and Barker 2011). The Q_S is the freshwater flux that is evaporation minus precipitation. The heat flux (Q_H) is the surface heat flux, which is the sum of short-/longwave radiations and sensible/latent heat flux. The local buoyancy flux (term in square brackets) is integrated over the surface area of the associated density bin $\Delta\sigma$, using a density bin width $\Delta\sigma = 0.1$ kg m^{-3}. The Π is a boxcar function with $\Pi = 1$ if σ is equal to the outcrop density (σ^*) and $\Pi = 0$ elsewhere. Here, the density is referenced to the surface since we are analyzing it at the surface (0 and 5 m) and subsurface depths (300 and 315 m) and in order to compare with other studies in the area (e.g., Desbruyères et al. 2019; Petit et al. 2021). The density fields are calculated according to the conventionally derived variable σ for seawater density [Intergovernmental Oceanographic Commission (IOC) et al. 2010]: $\sigma = \rho(S_A, \Theta) - 1000$ kg m^{-3}, where ρ is the density of a sample of seawater at Conservative Temperature Θ and Absolute Salinity S_A.

To estimate the SFWMT, we use monthly surface heat and freshwater fluxes from the fifth major global reanalysis produced by European Centre for Medium-Range Weather Forecasts (ERA5) atmospheric reanalysis (Hersbach et al. 2020). Surface temperature and salinity at 5-m depth are derived from EN4.2.2 (described in section 2a). ERA5 fluxes have 0.25°-grid resolution and were interpolated to EN4.2.2 grid (1°). We calculate the SFWMT for each month and subsequently determine the winter mean (January–April) for every year. Moreover, we sum the SFWMT within the eastern subpolar gyre (Fig. 1, black polygon). The area is defined based on mean winter SFWMT between 1950 and 2017 from EN4.2.2, for each density class from 27.0 to 27.5 kg m^{-3} (supplemental Fig. 3). Thus, we apply a third-order bandpass Butterworth filter with a cutoff period of 7–40 years (truncated ±3 years). We calculate the SFWMT only for 1947–2020. This is due to filter sensitivity since the inclusion of 2021 results in unrealistic anomalies at the edges.

c. *Complex empirical orthogonal function analysis*

To assess the propagation of thermohaline anomalies, we use a CEOF introduced by Horel (1984). The CEOF is a

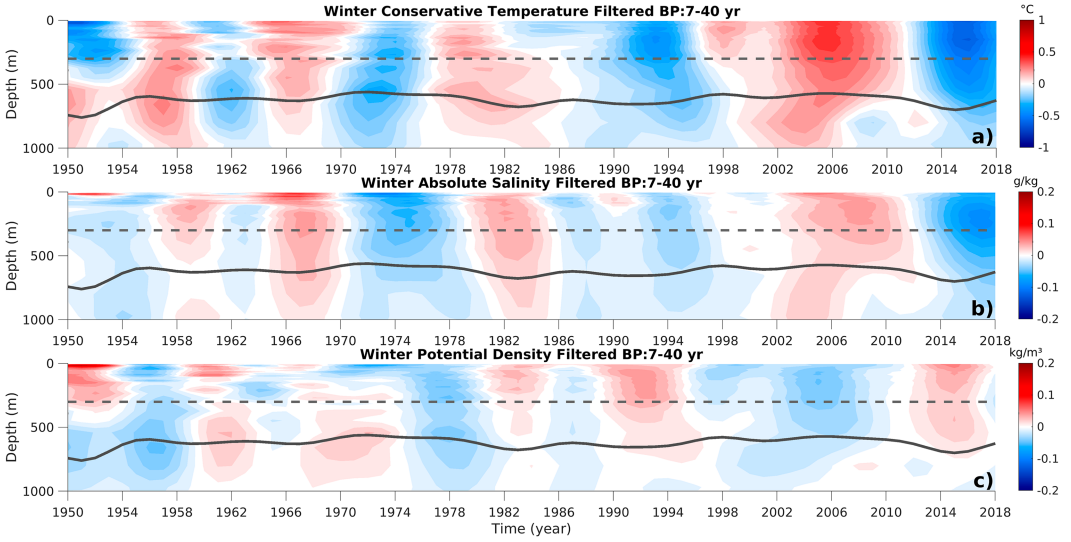

FIG. 2. EN4.2.2 average of the eastern subpolar region for (a) Conservative Temperature, (b) Absolute Salinity, and (c) density referenced to the surface. Anomalies are calculated for each layer relative to 1947–2021. A negative anomaly indicates values below the time average for that specific layer. The time series are filtered with a bandpass filter of 7–40 years (truncated ±3 years). The continuous dark gray line is the filtered mixed layer depth. The dashed gray line indicates a 300-m depth.

variant of the empirical orthogonal function (EOF). The EOF is useful for identifying spatial patterns of variability. The CEOF considers the time order of observations, which allows it to capture the evolving patterns and temporal variability in the dataset, providing a quantitative understanding of underlying oscillating mechanisms. The technique has previously been used to study thermohaline propagation in the North Atlantic by Furevik (2000) and Årthun et al. (2017).

A CEOF analysis was applied to the times series of temperature and salinity at each station of the SPNA-pathway (red) and the NS-pathway (purple) (Fig. 1) to derive the dominant signals and patterns of their variability (called modes). First, a third-order 7–40-yr bandpass Butterworth (truncated ±3 years) filter was applied to the time series of each station, resulting in a function $u_j(t)$. The filter size was chosen to focus on decadal time scales. After, a fast Fourier transform (FFT) was computed, generating both an imaginary and real part from the time series. Following this, the Hilbert transformation was performed by adding the imaginary part from the FFT $[\hat{u}_j(t)]$ to the original time series $[u_j(t)]$, producing a complex time series rotated by $\pi/2$ $[U_j(t)]$:

$$U_j(t) = u_j(t) + i\hat{u}_j(t), \tag{2}$$

where j denotes the station and t is the time. A singular value decomposition is calculated using $U_j(t)$, resulting in complex principal components [CPCs; Pn(t)] and CEOFs [Fn(x)]. The term $U_j(t)$ can thus be represented as a sum of the contribution from the N principal components:

$$U_j(t) = \sum_{n=1}^{N} P_n(t)F_n^*(j). \tag{3}$$

The variability explained by each CEOF mode is then calculated based on the variance explained by each principal component. Here, we calculate six principal components ($N = 6$) and then estimate the anomalies' propagation velocity based on the first mode of variability. The velocity is found by using the distance and time for an anomaly to travel from the first station until the last station of each pathway. The time lags used for the velocity calculation are found using the ±0.25 standard deviation threshold of the CEOF number 1 of temperature and salinity at 315 m from EN4.2.2. The velocity is calculated for each cold–fresh and warm–salty anomaly, and then, their mean is considered.

d. *Cross correlation*

We calculate a standard cross correlation for each density class to assess the relationship between decadal SFWMT and temperature anomalies. The calculation was made using ±20 lag years and the temperature (at 315 m) of NS-st2. The cross correlation was calculated for filtered SFWMT and temperature with third-order 7–40-yr bandpass Butterworth truncated ±3 years. The significance level is calculated by the standard two-sided Student's t test (O'Mahony 1986) at 90% and does not account for auto- and cross covariances.

3. Results

a. *Variability of surface-forced water mass transformation*

Ocean temperature in the eastern subpolar gyre (Fig. 1) is associated with pronounced decadal variability with warm and cold anomalies, extending over the upper 500–1000 m (Fig. 2a). Overall, warm anomalies are characterized by positive

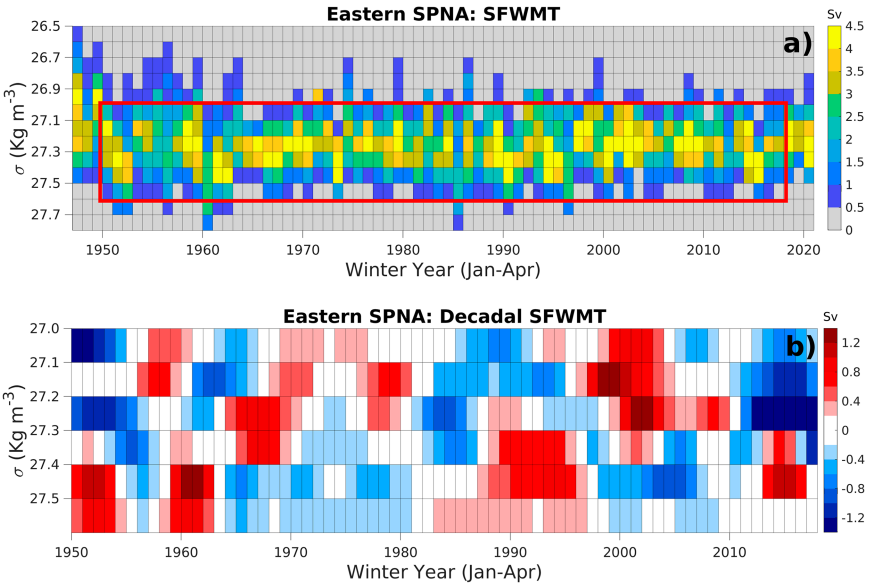

FIG. 3. (a) SFWMT in the eastern subpolar gyre during winter, with a density class interval of 0.1 kg m^3 from 1947 to 2021. The red rectangle highlights the time period and density interval shown in (b). (b) Filtered SFWMT anomaly for each density class, using a bandpass filter for 7–40 years (truncated ±3 years). Positive anomalies represent SFWMT values exceeding the time average, while negative anomalies mean values below the time average SFWMT.

salinity anomalies (Fig. 2b). The main contributor to density anomaly is the variation of temperature. However, the temperature and salinity anomalies are partly density-compensated. Density anomalies are generally in phase with the thermohaline anomalies between 1975 and 1990, a period in which salinity appears to drive most of the density variability (Fig. 2c). On the other hand, after the mid-1990s, a shift occurred: a negative anomaly in both temperature and salinity leads to a positive density anomaly, which indicates that temperature is the main driver.

We show the SFWMT during boreal winter for density classes ranging from 26 to 27.9 kg m^{-3}, with intervals of 0.1 kg m^{-3} in Fig. 3a. Most of the winter SFWMT occurs within the density classes 27.0 and 27.5 kg m^{-3}. When computing the time average for each density class, the 27.1 kg m^{-3} class exhibited the highest average of 3.6 Sv (1 Sv ≡ 10^6 m^3 s^{-1}), while the 27.5 kg m^{-3} class displayed the lowest average of 0.8 Sv. The SFWMT exhibits high year-to-year variability within each density class during winter. The results discussed in this section focus on SFWMT values exceeding the threshold of 0.5 Sv.

The decadal variability of winter SFWMT accounts for 32% of the interannual variability as shown in Fig. 3b. The calculation is directly proportional considering the maximum SFWMT (Fig. 3a) and the absolute value of the maximum decadal anomaly (Fig. 3b). Here, we consider 27.0–27.2 kg m^{-3} as light-density classes, while 27.3–27.5 kg m^{-3} as denser-density classes. During the 1980s and 1990s, positive anomalies in denser layers varied from 0.2 to 1.0 Sv (Fig. 3b). During this period, the positive anomalies lasted approximately 2 times longer than in other decades (27.4 kg m^{-3}: 1987–95). Following this prolonged event, the subsequent period from 1996 to 2004 shows the emergence of longer and more intense positive anomalies in the lighter-density classes (27.0–27.2 kg m^{-3}). Figure 3b shows a recurring pattern throughout the analyzed period when denser water transformation (>27.3 kg m^{-3}) is strong and lighter water transformation (<27.3 kg m^{-3}) is weak, and vice versa.

The cross correlation between decadal SFWMT of lighter and denser classes shows a significant negative correlation between 27.2 and 27.4 kg m^{-3} (27.5 kg m^{-3}) of −0.58 and −0.65, respectively, at a time lag of 0 year (Fig. 4). Interestingly, Fig. 4 also displays around the same correlation values at a time lag of −1 year, suggesting that denser classes lead to the opposite changes in lighter classes in the next year. Considering this, the end of a cold–fresh period with positive anomalies in denser classes (27.4–27.5 kg m^{-3}) will be followed by stronger positive anomalies in the light class 27.2 kg m^{-3} only after two winters. This suggests a combined evolution of the SFWMT anomalies between different density classes within the eastern subpolar gyre.

Variations in the SFWMT can be driven by both surface buoyancy fluxes and the area covered by a particular surface density range. We have analyzed the influence of surface fluxes on the decadal SFWMT anomalies in the eastern subpolar gyre from density class 27.1 until 27.5 kg m^{-3} (Figs. 5a–e). This has been done by keeping the surface fluxes and the surface density constant (climatology) during the SFWMT calculation. We observed that surface fluxes impact the amplitude of the SFWMT, especially within the range of classes 27.0–27.3 kg m^{-3}. The influence of surface fluxes on the amplitude decreases for classes 27.4–27.5 kg m^{-3}. This result is consistent with previous findings by Petit et al. (2021) and Årthun (2023), highlighting the

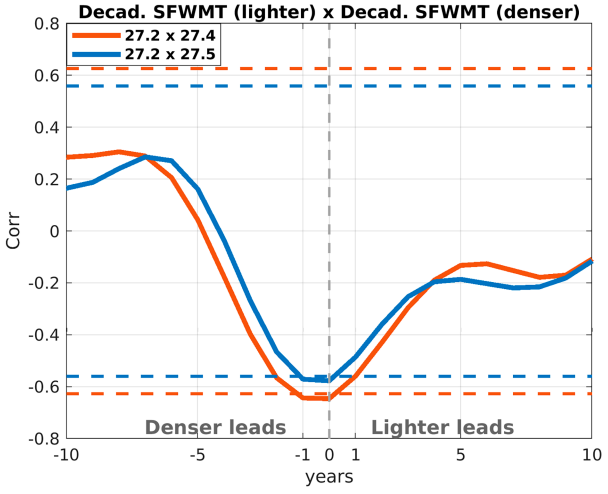

FIG. 4. Cross correlation between bandpass filtered winter SFWMT between the classes 27.2 and 27.4 kg m^{-3} in orange and between the classes 27.2 and 27.5 kg m^{-3} in blue. The dashed lines are the respective significant correlations at the 95% level by the standard two-sided Student's t test. The calculation considers autocorrelation, and all time series are previously detrended.

dominant role of upper-ocean hydrography in driving the variability of the SFWMT in the region. Given the significant role of ocean hydrography in the eastern subpolar gyre, our investigation now focuses on studying the propagation of thermohaline anomalies along the Atlantic Water pathways, which contribute to downstream predictability.

b. *Propagation of decadal thermohaline anomalies*

After crossing the eastern subpolar gyre, the propagation of thermohaline anomalies follows two main routes: the NS-pathway (Fig. 1, purple), which crosses the Iceland–Scotland Ridge; and the SPNA-pathway (Fig. 1, red), which passes through the Reykjanes Ridge. Our analysis primarily focuses on the differences and similarities between the two pathways regarding the subsurface propagation of thermohaline anomalies, specifically at a depth of 300 m. We chose to analyze around 300 m since, along the SPNA-pathway, the core of the Atlantic Water is in the subsurface in the Irminger Sea and beyond. Thus, by tracking the anomalies in the subsurface, we can actually track anomalies entering the subpolar gyre. Consequently, in the SPNA-pathway, a consistent propagation of anomalies is only found in the subsurface. Considering this, in each dataset, we selected the closest depth to 300 m: 315 m for EN4.2.2 and 300 m for Ishii.

In Fig. 2, we showed that thermohaline anomalies at the surface extend beyond 315 m on a decadal time scale. Below, we present CEOF results from EN4.2.2 in the subsurface, whereas additional CEOF analysis for all datasets at the surface (0 and 5 m) is available in the supplemental material (supplemental Figs. 4 and 5). In this work, we thus expand the analysis made by Årthun et al. (2017) by testing the surface and subsurface for three different datasets, increasing the analyzed period, and introducing another branch toward the SPNA.

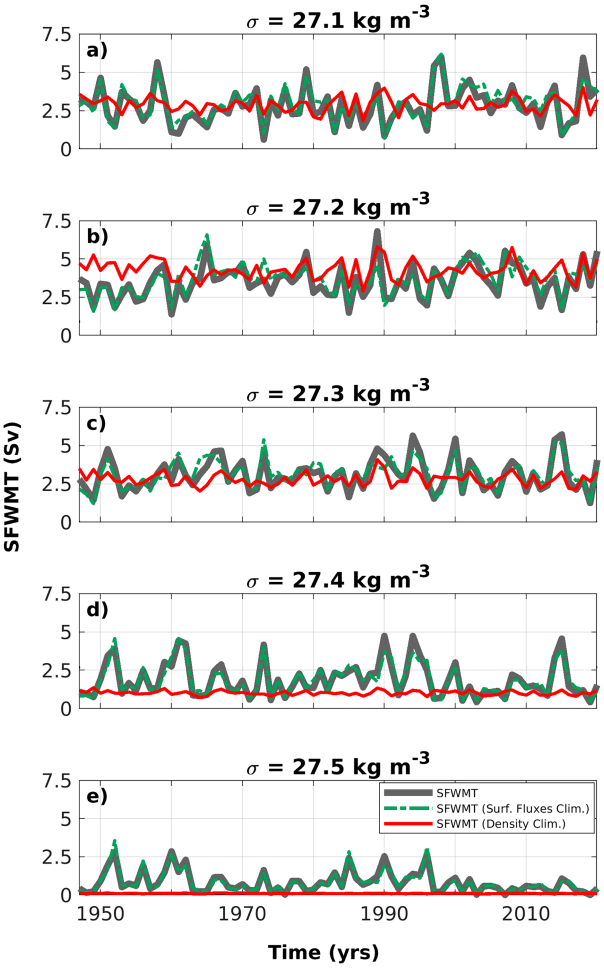

FIG. 5. Winter SFWMT time series presenting the accumulated sum within the eastern subpolar gyre for various density classes: (a) 27.1, (b) 27.2, (c) 27.3, (d) 27.4, and (e) 27.5 kg m^{-3}. The thick gray line represents the SFWMT. The green dashed line shows the SFWMT calculated based on surface fluxes' climatology, while the continuous red line displays the SFWMT calculated considering the climatology of surface density. The climatology of surface fluxes and surface density is computed between 1947 and 2020.

Figures 6a and 6c show the first mode of variability for temperature and salinity along the NS-pathway, respectively. The CEOF's leading mode of subsurface temperature (315 m) explains 52% of its variability, while the CEOF's leading mode of subsurface salinity explains 76% of the variability in the NS pathway. We generally find alternating periods of warm and cold anomalies at the stations, repeating throughout the 74-yr-long record with four warm–salty and cold–fresh cycles after 1950. When comparing anomalies at the first and last stations, there is a time lag between them, which indicates propagation.

The amplitude of the decadal temperature and salinity anomalies is shown in supplemental Fig. 6, which shows the bandpass filtered time series from stations along the NS-pathway (no CEOF analysis is applied). For temperature anomalies, there is an overall weakening of the amplitude close to the Iceland–

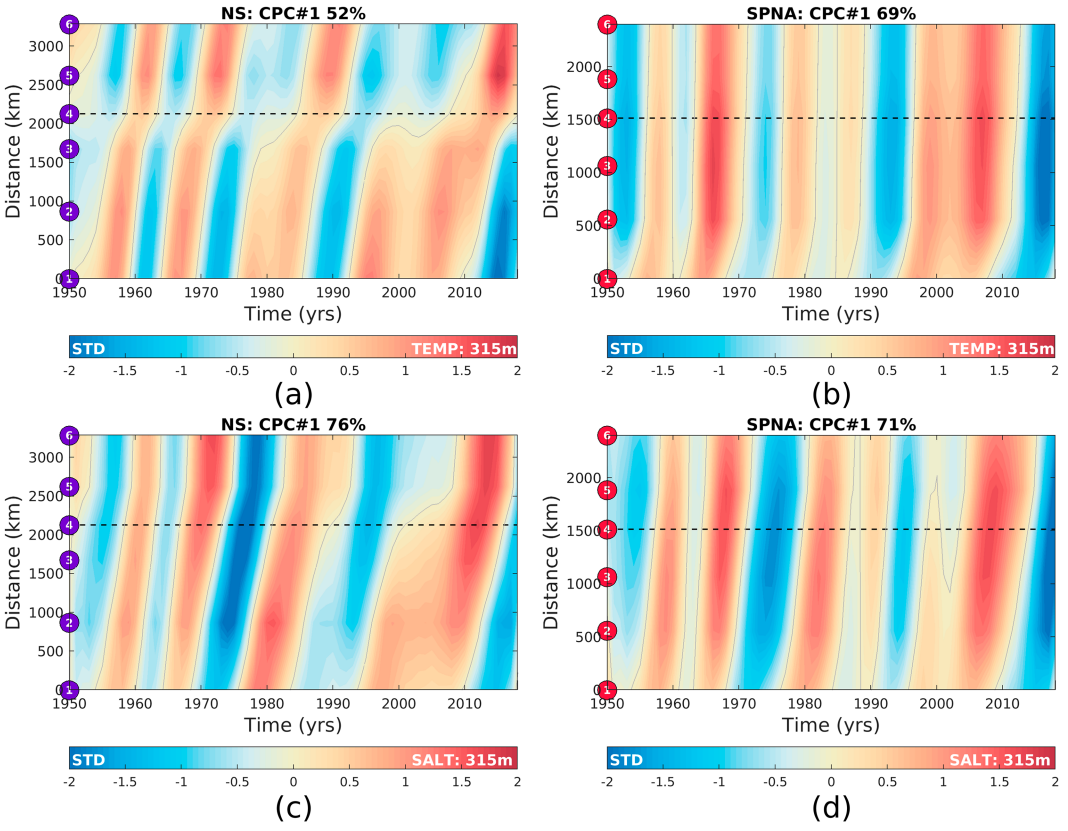

FIG. 6. The first leading mode of subsurface winter temperature for the (a) NS stations and (b) SPNA stations, along with the first leading mode of subsurface winter salinity for the (c) NS stations and (d) SPNA stations. The analysis utilizes EN4.2.2 data. The *y* axis is the geographical distance between the NS-st1 (SPNA-st1) and NS-st6 (SPNA-st1), while the *x* axis is the time evolution. Colors indicate the standard deviation for positive and negative anomalies. The dashed lines represent the (a),(c) Iceland–Scotland Ridge for the NS and the (b),(d) Reykjanes Ridge for the SPNA. Zero contours are shown as gray lines. The percentage of variability explained by the first mode of the CPC is provided in the title.

Scotland Ridge (NS-st4). NS-st4 also shows an overall reduced variability between warm–salty and cold–fresh periods (Fig. 9b). The Iceland–Scotland Ridge is relatively shallow compared to the surrounding basins, and the topography and circulation patterns around the ridge are complex. The Atlantic inflow across the ridge is characterized by high mesoscale activity, leading to high transport variability (Sherwin et al. 2006; Zhao et al. 2018), which masks the advection of thermohaline anomalies on interannual to decadal time scales (Asbjørnsen et al. 2019). From the 1990s until the end of the 2000s, we find a double warm–salty anomaly upstream of the Iceland–Scotland Ridge (NS-st1–NS-st4) and a double cold–fresh anomaly in the stations inside the Norwegian Sea. The results are consistent in the CEOF analysis and the filtered time series. We refer to the prolonged warm–salty (cold–fresh) period as "double" since they do not meet our defined threshold for an anomaly (± 0.25 standard deviation) due to their lower amplitude to be defined as one single anomaly.

Following the SPNA-pathway, the CEOF's leading mode accounts for 69% of the temperature variability (Fig. 6b). The decadal variability of temperature and salinity in the SPNA-pathway is similar to the one described by the leading mode of the NS-pathway, specifically, a consistent occurrence of one warm–salty and one cold–fresh anomaly approximately every decade from the 1950s to the 1980s, including the double pattern between the 1990s and the 2000s.

In contrast to the NS-pathway, the SPNA-pathway exhibits temperature anomalies with small time lags. Salinity anomalies, however, show similar time lags in both pathways (Figs. 6c,d). The CEOF's leading mode of subsurface salinity in the SPNA-pathway explains 71% of the variability (Fig. 6d). The periods of cold–fresh anomalies identified by the CPC#1 in the SPNA-pathway align with the well-documented Great Salinity Anomaly (GSA) events reported in the literature (Belkin et al. 1998; Belkin 2004; Holliday et al. 2020). The bandpass filtered time series have the same pattern of variability of the CEOF for temperature and salinity (supplemental Fig. 6). Introducing additional stations to trace the anticyclonic gyre around the Reykjanes Ridge within the SPNA-pathway reveals the same pattern of warm–salty and cold–fresh anomalies and their respective speeds (not shown). Despite that, the addition of stations along the anticyclonic pathway increases the CEOF's first

TABLE 2. Average travel time and speed of temperature and salinity anomalies propagating along the NS-pathway and SPNA-pathway at a depth of 315 m for the EN4.2.2 dataset are provided. The corresponding estimates for the Ishii dataset are enclosed in parentheses. The different numbers of warm–salty and cold–fresh anomalies were considered in a weighted average.

	Mean arrival time (years)		Average speed (cm s^{-1})	
Anomaly	Temperature	Salinity	Temperature	Salinity
NS-pathway	10 (6.8)	7.9 (5.2)	1 (1.5)	1.3 (2)
SPNA-pathway	2.8 (3.4)	4.6 (2.4)	2.2 (1.8)	1.4 (2.6)

mode of variability from 69% to 75% for temperature and from 71% to 76% for salinity.

In summary, the analysis of the NS-pathway and SPNA-pathway reveals similarities in the propagation of temperature and salinity anomalies. The first mode of temperature and salinity variability for both pathways explains more than 50% of the total variance, indicating their significance in capturing the overall variability. Moreover, the NS-pathway exhibits longer time lags from the first to the last station compared to the SPNA-pathway, particularly for temperature. This suggests that temperature anomalies have a faster propagation rate in the SPNA-pathway (Table 2), which is relevant for predictability in the area. These findings highlight both the similarities and differences between the two pathways. However, an important question remains: How do these specific characteristics relate to the SFWMT in the eastern subpolar gyre?

c. *The relation between the decadal thermohaline variability and surface forcing*

The variability of thermohaline anomalies carried by the Atlantic Water through the NS-pathway is seen in Fig. 7. The table presents information regarding the arrival and end of each temperature anomaly from NS-st1 to NS-st6, along with the decadal SFWMT anomaly in the eastern subpolar gyre (during cold and warm anomalies at NS-st2). For instance, a warm anomaly occurred in the eastern subpolar gyre in the 1950s ("Warm50") reaches the stations after the Iceland–Scotland Ridge during the 1960s. During the Warm50, the Norwegian Sea exhibits anomalies with the opposite signal ("Cold 50"). Based on this, each anomaly event is named according to its signal before and after the Iceland–Scotland Ridge.

Looking into the decadal SFWMT anomaly (Fig. 3c), we see that positive SFWMT anomalies in lighter classes (27.0–27.2 kg m^{-3}) are associated with warm anomalous periods in the eastern subpolar gyre (Fig. 7; NS-st2) and happen once every decade (e.g., during the 1950s, 1960s, 1980s, 1990–2000s), except after the 2010s. In the denser classes (27.4–27.5 kg m^{-3}), positive anomalies happen once every decade, except during the 1970s and 2000s, and generally are associated with cold anomalous periods (Fig. 7; NS-st2).

To assess the relationship between decadal SFWMT in the eastern subpolar gyre and propagation of thermohaline anomalies, we have focused on temperature variability at NS-st2 (Fig. 1, purple). We selected NS-st2 for comparison since it is within the eastern subpolar gyre (black polygon), where most of the SFWMT between 27.0 and 27.5 kg m^{-3} happens (supplemental Fig. 3).

The cross-correlation analysis shows a significant positive correlation at zero time lag for light-density classes (27.1–27.2 kg m^{-3}) and a significant negative correlation for denser classes (27.4–27.5 kg m^{-3}) at zero and one-year time lag (Fig. 8a). We have analyzed all density classes in the interval 26.0–27.9 kg m^{-3}, and here, we show only the results for the significant correlations. The results from the cross correlation suggest that when a warm anomaly (lighter water) enters the eastern subpolar gyre, more SFWMT occurs in light-density classes (positive correlation). In contrast, when a cold anomaly (denser water) enters the eastern subpolar gyre, more SFWMT occurs in denser classes (negative correlation). For denser water masses, the SFWMT seems to lead temperature changes by 1 year. This one-year delay in denser classes is explained by a one-year delay between surface and subsurface temperature variability.

In Figs. 8b–e, we compare the temperature anomalies at NS-st2 and decadal SFWMT for the four significant density

	Warm50	Cold60	Warm60	Cold70	Warm80	Cold80	Warm90	Warm00	Cold10
NS-St1	1954-58	1961-63	1965-68	1970-74	1976-84	1986-91	1993-2007		2011-18
NS-St2	1956-59	1961-64	1966-69	1971-76	1978-86	1988-93	1995-2012		2014-18
NS-St3	1957-60	1962-65	1967-71	1973-77	1983-87	1989-94	1997-99	2004-14	2015-18
SFWMT-27.2	-0.2	-0.5	3.3	-0.5	-2.7	0.4	4.8		-7.7
SFWMT-27.4	0.1	1.8	-1.4	-1.9	-0.7	3.9	-6		2.9
Iceland-Scotland Ridge									
	Cold50	**Warm60**	**Cold60**	**Warm70**	**Cold70**	**Warm80**	**Cold90**	**Cold00**	**Warm10**
NS-St4	1956-57	1960-62	1965-67	1970-73	1976-78	1987-90	1993-97	2004-05	2012-17
NS-St5	1956-59	1960-63	1965-68	1970-75	1977-85	1987-92	1994-2008		2012-18
NS-St6	1957-60	1961-64	1966-70	1972-76	1978-88	1988-93	1995-2012		2014-18

FIG. 7. Warm and cold anomaly periods for the NS stations. Decadal SFWMT (Sv) in the classes 27.2 (light) and 27.4 kg m^{-3} (dense) within the eastern subpolar gyre. The definition of warm and cold periods is based on the CEOF number 1 of temperature at 315 m from EN4.2.2, using $-0.25 < \text{STD} > 0.25$ for all stations.

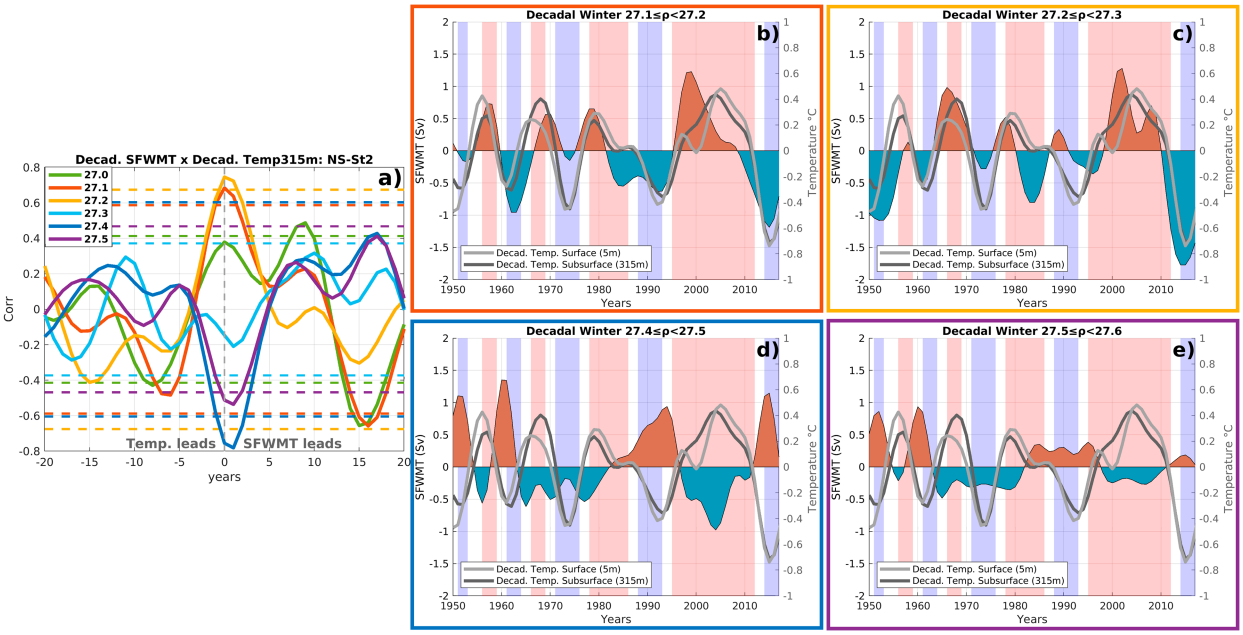

FIG. 8. (a) Cross correlation between bandpass filtered winter SFWMT (only density classes with significant correlation) and the decadal surface and subsurface temperature anomaly at NS-st2. The dashed lines are the respective significance levels of each density class. The calculation considers autocorrelation, and all time series are previously detrended. The decadal SFWMT for the density classes (b) 27.1, (c) 27.2, (d) 27.4, and (e) 27.5 kg m^{-3}. (b)–(e) The decadal temperatures of NS-st2 at the surface and subsurface are in light gray and dark gray, respectively. The hatched red and blue areas correspond to periods of positive and negative subsurface temperature anomalies, respectively, based on the periods defined by the first CEOF mode of variability.

classes 27.1–27.2 and 27.4–27.5 kg m^{-3}. In addition, we show temperature anomalies both at the surface (light gray) and subsurface (dark gray). The analysis shows similar results for the surface and subsurface: approximately in phase with the SFWMT for the light layers 27.1–27.2 kg m^{-3} (Figs. 8b,c) and negatively correlated with the SFWMT for the denser layers 27.4–27.5 kg m^{-3} (Figs. 8d,e). The comparison in these figures also includes periods of positive and negative temperature anomaly propagation through NS-st2 (CEOF number 1) in areas hatched in red and blue, which are also in phase and out of phase with the respective density classes described above. Despite the overall correlation, there are periods when the correlation breaks down, for instance, during 1970–75 in dense classes and between the 1980s and 1990s in the light classes (27.1–27.2 kg m^{-3}). Both periods are associated with stronger GSA events (Belkin 2004).

Furthermore, we investigate how the Atlantic Water changes as it travels northward. We analyze the surface temperature and salinity properties during warm–salty and cold–fresh periods (as defined in section 3b). The transformation of Atlantic Water in the eastern subpolar gyre (between NS-st1 and NS-st4) is seen in a temperature and salinity (TS) diagram (Fig. 9). On average, during a warm–salty period, the Atlantic Water becomes approximately 1°C colder and 0.13 PSU saltier, with a standard deviation of ±0.3°C and ±0.01 PSU at NS-st4 (Figs. 9a,b: red). During a cold–fresh period, the Atlantic Water becomes around 0.7°C colder and 0.15 PSU saltier, with a standard deviation of ±0.14°C and ±0.02 PSU at NS-st4 (Figs. 9a,b, blue).

In addition, we find that within the warm–salty periods, NS-st4 (Fig. 9b) exhibited less salinity variability compared to NS-st1 (Fig. 9a), while the opposite trend was observed for temperature. The differences between warm–salty and cold–fresh periods are smaller at NS-st4 than at NS-st1. This overall reduced variability at NS-st4 in Atlantic Water properties suggests an overall weakening of the thermohaline anomaly signal at NS-st4. The transformation of Atlantic Water in the eastern subpolar gyre (between NS-st1 and NS-st4) might be due to advection, mixing, as well as SFWMT. Nevertheless, we could not identify the causes of the weakening of the anomalies with our analysis. Although there is a weak relationship between the decadal anomalies and the North Atlantic Oscillation (NAO) and surface net fluxes (Årthun et al. 2017), atmospheric forcing can, in certain periods, modify these anomalies (Furevik 2001; Holliday et al. 2008; Carton et al. 2011).

4. Discussion

This paper examines the relationship between decadal thermohaline anomalies and SFWMT in the eastern subpolar gyre. Our primary objective is to understand the extent to which these thermohaline anomalies are reflected in SFWMT processes. In addition to that, we compare the propagation of thermohaline anomalies in two distinct pathways after they cross the eastern subpolar gyre. By examining these pathways, we can identify similarities and differences in the behavior of thermohaline anomalies, which contributes to

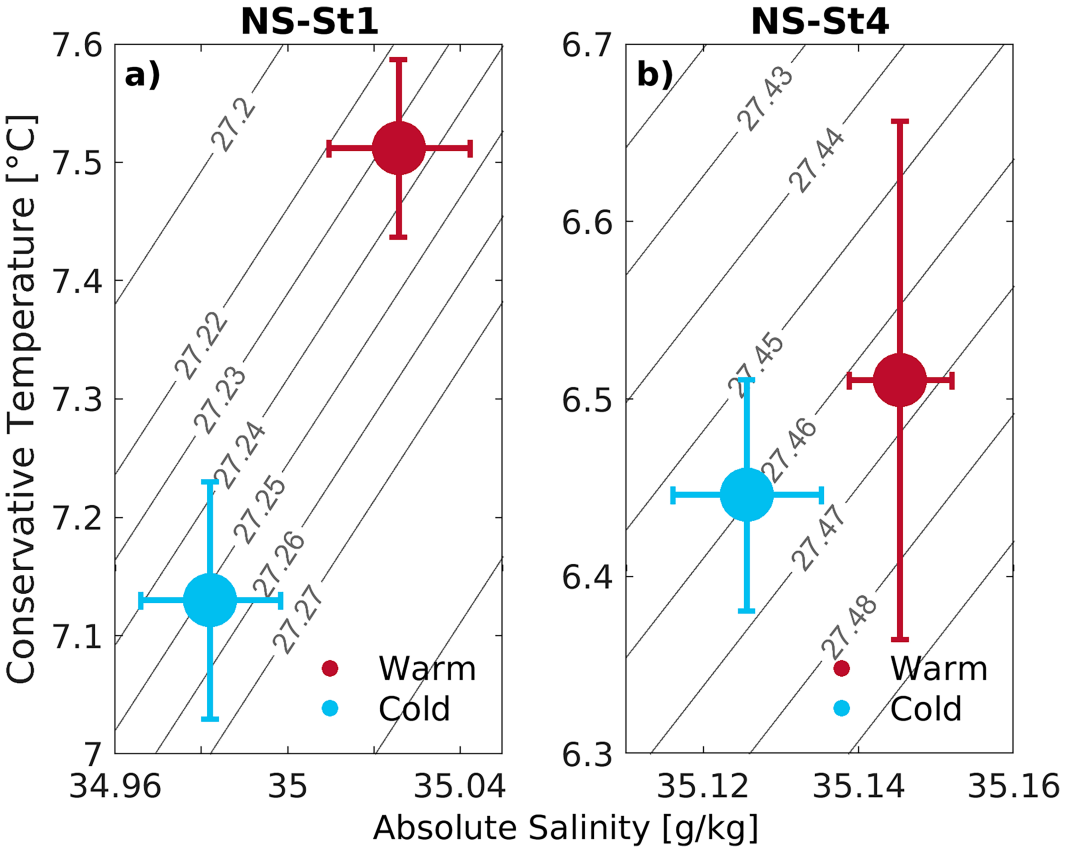

FIG. 9. Mean temperature–salinity properties during winter for warm–salty (red) and cold–fresh (blue) periods: (a) NS-st1 (before eastern subpolar gyre) and (b) NS-st4 (after eastern subpolar gyre). The error bar shows the standard deviation for temperature in the vertical and salinity in the horizontal.

a better understanding of climate variability in the North Atlantic region.

Our findings indicate a significant correlation between thermohaline anomalies and decadal SFWMT variability in the eastern subpolar gyre, with surface fluxes playing a minor role. When a warm and saline anomaly enters the region, it leads to positive SFWMT anomalies in light-density layers. However, the arrival of a cold and fresh anomaly does not consistently result in positive SFWMT anomalies in denser layers. For instance, during the Cold70 event (Fig. 7), SFWMT anomalies were positive for light layers but negative for denser layers (Fig. 3c). Interestingly, this is the only period that shows a negative density anomaly during a cold–fresh event (Fig. 2c), suggesting that an assumed direct relationship between cold–fresh events and higher SFWMT in denser layers may not always hold. This is likely due to salinity dominating the density changes during the Cold70.

Our results show that surface density controls the variability of the SFWMT on decadal time scales, which agrees with the analysis of Petit et al. (2021). However, surface fluxes seem to play a role in driving the SFWMT on short time scales, for instance, in the event of a cold blob from 2012 to 2016 (e.g., Josey et al. 2018; Holliday et al. 2020). Moreover, based on a different methodology than SFWMT and model results, Robson et al. (2012) found surface fluxes as the main driver of decadal water mass transformations in the subpolar North Atlantic.

On multiannual to decadal time scales, changes in surface density are suggested to be determined by ocean advection in the eastern subpolar gyre (Piecuch et al. 2017; Foukal and Lozier 2018). Our results demonstrate that hydrographic variability exerts a significant influence on decadal-scale SFWMT variability. This influence might have implications for the variability of the lower limb of AMOC, as the eastern subpolar gyre, together with the Irminger Sea, plays a prominent role in determining the strength of AMOC in the subpolar North Atlantic (Fu et al. 2020).

Fraser and Cunningham (2021) attribute the low-frequency variability of AMOC to large-scale density anomalies. Consistent with this finding, a comparison between an AMOC reconstructed using SST (Caesar et al. 2021) and an average of the SFWMT of classes 27.3 and 27.4 kg m^{-3} shows a significant correlation of 0.45 (Fig. 10). Since our analysis focuses only on the eastern subpolar gyre, surface fluxes are expected to drive the diapycnal fluxes with little or no lag (Petit et al. 2020). The highest correlation was found by combining the density classes 27.3 and 27.4 kg m^{-3}. We chose these density classes since the transformation across 27.35 kg m^{-3} provides

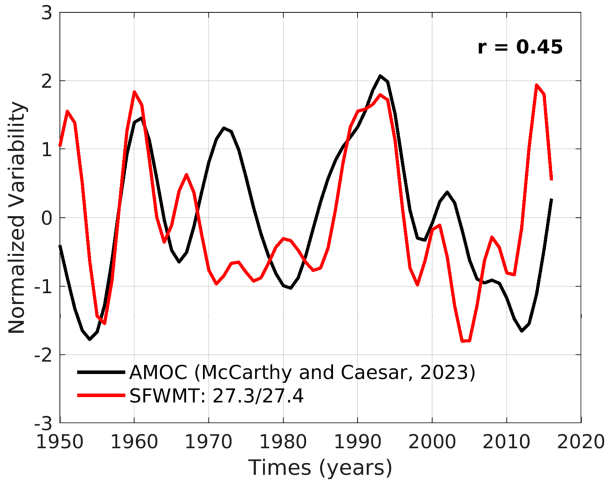

FIG. 10. Normalized variability of AMOC reconstruction (McCarthy and Caesar 2023) and the average SFWMT of classes 27.3 and 27.4 kg m^{-3}. The correlation between the two time series is significant at the 99% confidence level. Both time series were filtered with a bandpass filter of 7–30 years.

critical preconditioning for the deep waters of the AMOC lower limb (Brambilla et al. 2008; Thierry et al. 2008; Petit et al. 2020). In contrast, an investigation based on monthly results suggests a weak connection between AMOC changes and hydrography variations, which were more related to surface fluxes redistributions by the subpolar gyre (Fu et al. 2020).

The investigation of the decadal thermohaline anomalies along the NS-pathway reveals a consistent propagation pattern similar to previous studies (Yashayaev and Seidov 2015; Årthun et al. 2017), indicating an average lag time of approximately 10 years from the North Atlantic to the Arctic. Focusing on the winter season, our analysis shows comparable average speed rates for salinity and temperature, measuring 1.3 and 1.0 cm s^{-1}, respectively, at a depth of 315 m (see Table 2). However, notable disparities between salinity and temperature arise in their respective first modes of variability. In the NS-pathway, the first CEOF mode exhibits salinity variability that is 24% higher than temperature, while the SPNA-pathway shows similar variability for both variables. This difference in the first mode of variability between salinity and temperature has implications for climate predictability, particularly in the Norwegian Sea. Notably, sea surface salinity showed higher predictive skill than sea surface temperature in four out of five model versions examined by Passos et al. (2023). Moreover, observational analysis suggests that air–sea heat fluxes in the Norwegian Sea can restrict the predictability associated with poleward temperature anomalies (Asbjørnsen et al. 2019).

In the SPNA-pathway, salinity variability shows similar patterns to the NS-pathway (Figs. 6c,d). At the surface, temperature results from HadISST show propagation only from SPNA-st1 to SPNA-st5, which might be related to the presence of cold and fresh Arctic Water close to the eastern Greenland coast (SPNA-st6) (supplemental Fig. 4a). In contrast, in EN4.2.2, no time lag is observed from SPNA-st1 to Reykjanes Ridge (SPNA-st4) on a decadal time scale (supplemental Fig. 4c). The Ishii dataset shows propagation at the surface and is overall similar to the other datasets (supplemental Fig. 4e). In the subsurface, temperature propagates 2 times faster (EN4.2.2) in the SPNA-pathway than in the NS-pathway, with a time lag of 2.8 years for EN4.2.2 and 3.4 years for Ishii. Along the SPNA-pathway, the average speed rate for salinity is 1.4 cm s^{-1}, while temperature is faster: 2.2 cm s^{-1}. However, this result is not seen in the Ishii dataset, where we found an average speed rate for salinity faster than for temperature (Table 2). Previous research by Yashayaev and Seidov (2015) noted significant differences in the propagation rates of salinity and temperature anomalies in the Nordic seas. These authors attribute this difference to the leading role of horizontal advection in salinity anomaly propagation, while the temperature is additionally influenced by competing air–sea interactions along the Atlantic Water pathway. Our results, however, do not show a significant average speed difference in the subsurface for the NS-pathway, and it is inconclusive for the SPNA-pathway.

The CEOF patterns show normalized thermohaline anomalies along the two pathways. However, it is important to note that the amplitude of the anomalies varies along these pathways (bandpass filtered time series in supplemental Fig. 6). This variation in amplitude may be associated with surface flux variability (see supplemental Fig. 7). The SPNA-pathway generally exhibits a pattern where surface flux variability aligns with the thermohaline anomalies. This alignment implies that warm anomalies are accompanied by positive heat and freshwater flux, indicating heat transfer from the ocean to the atmosphere and higher evaporation than precipitation. In contrast, in the NS-pathway, the similarity between the surface flux variability and the thermohaline anomalies is only observed upstream of the Iceland–Scotland Ridge.

This study focused on ocean variability in the eastern subpolar gyre region. Given the proximity of the NS-pathway and SPNA-pathway in this region, their thermohaline variability exhibits similarities. However, as we move downstream from the eastern subpolar gyre, where the pathways diverge, noticeable differences between the two pathways emerge, as described above.

5. Summary

In our study, we use observation-based data to describe the relationship between the propagation of thermohaline anomalies and surface-forced water mass transformation (SFWMT) in the eastern subpolar gyre on decadal time scales. First, we found that the surface-forced water mass transformation in the eastern subpolar gyre showed pronounced decadal variability. This variability is associated with the variability of temperature and salinity anomalies. The results suggest that when a warm anomaly enters the eastern subpolar gyre, more SFWMT occurs in light-density classes. In contrast, when a cold anomaly enters the eastern subpolar gyre, more SFWMT occurs in denser classes. Variability in the heat and freshwater fluxes in the eastern subpolar gyre has a small influence on

the decadal variations of the SFWMT (keeping the fluxes constant gives approximately the same decadal variations in the SFWMT).

Second, we investigated thermohaline anomalies on a decadal time scale along two pathways: one branch within the subpolar North Atlantic, entering the western subpolar gyre (SPNA-pathway), and another branch, crossing the Iceland–Scotland Ridge toward the Fram Strait (NS-pathway). Thermohaline anomalies seem to follow the two Atlantic Water pathways, being visible at the surface and subsurface in the NS-pathway and only in the subsurface in the SPNA-pathway. For both routes, we generally find alternating periods of warm and cold subsurface anomalies at the stations, repeating throughout the 74-yr-long record with four warm-salty and cold–fresh periods after the 1950s. The cold–fresh periods are similar to the Great Salinity Anomaly events described by the literature in the SPNA (Belkin et al. 1998; Belkin 2004; Holliday et al. 2020). Moreover, the propagation of thermohaline anomalies is faster in the SPNA than in the Norwegian Sea, especially for temperature.

The variability of thermohaline conditions in the eastern subpolar gyre plays an important role in driving the SFWMT, particularly within the density classes 27.1–27.2 and 27.4–27.5 kg m^{-3}. These hydrographic changes are closely related to the propagation of thermohaline anomalies along the Atlantic Water pathways. As a result, the variability of AMOC in this region might exhibit predictability. It is worth noting that the SFWMT connects the upper ocean with intermediate/deep layers, ultimately influencing the lower limb of the AMOC. Considering the eastern subpolar gyre's contributions to AMOC (Lozier et al. 2019; Petit et al. 2020), understanding the variability of thermohaline anomalies in this region might have implications for predicting AMOC's variability, which, in turn, is important for predicting the climate of western Europe and North America (Collins and Sinha 2003; Jacob et al. 2005; Yin and Zhao 2021).

Acknowledgments. LP, HL, and MÅ received funding from the Trond Mohn Foundation through the Bjerknes Climate Prediction Unit (BFS2018TMT01). HRL has received funding from the Research Council of Norway through the JPI Climate/JPI Oceans NextG-Climate Science-ROADMAP (Grant 316618/JPIC/JPIO-04), and MÅ has received funding from the Bjerknes Centre for Climate Research (project DYNASOR). The U.S. National Science Foundation funds FS through OSNAP Projects (Grants 1756272 and 1948482).

Data availability statement. All data used in this study are available online, and it can be accessed as follows: EN4-climatology (https://www.metoffice.gov.uk/hadobs/en4/download-en4-2-2.html, last accessed on 11 February 2022); ERA5 reanalysis (https://cds.climate.copernicus.eu/cdsapp#!/dataset/reanalysis-era5-single-levels-monthly-means?tab=form, last accessed on 9 March 2023); Met Office Hadley Centre Sea Ice Sea Surface Temperature dataset (https://www.metoffice.gov.uk/hadobs/hadisst/data/download.html, last accessed on 21 March 2022); and Ishii Ocean Analyses Project dataset (https://rda.ucar.edu/datasets/ds285.3/, last accessed on 4 October 2022).

REFERENCES

Alexander, M. A., and C. Deser, 1995: A mechanism for the recurrence of wintertime midlatitude SST anomalies. *J. Phys. Oceanogr.*, **25**, 122–137, https://doi.org/10.1175/1520-0485(1995)025<0122:AMFTRO>2.0.CO;2.

Årthun, M., 2023: Surface-forced variability in the Nordic Seas overturning circulation and overflows. *Geophys. Res. Lett.*, **50**, e2023GL104158, https://doi.org/10.1029/2023GL104158.

——, T. Eldevik, L. H. Smedsrud, Ø. Skagseth, and R. B. Ingvaldsen, 2012: Quantifying the influence of Atlantic heat on Barents Sea ice variability and retreat. *J. Climate*, **25**, 4736–4743, https://doi.org/10.1175/JCLI-D-11-00466.1.

——, ——, E. Viste, H. Drange, T. Furevik, H. L. Johnson, and N. S. Keenlyside, 2017: Skillful prediction of northern climate provided by the ocean. *Nat. Commun.*, **8**, 15875, https://doi.org/10.1038/ncomms15875.

Asbjørnsen, H., M. Årthun, Ø. Skagseth, and T. Eldevik, 2019: Mechanisms of ocean heat anomalies in the Norwegian Sea. *J. Geophys. Res. Oceans*, **124**, 2908–2923, https://doi.org/10.1029/2018JC014649.

Belkin, I. M., 2004: Propagation of the "Great Salinity Anomaly" of the 1990s around the northern North Atlantic. *Geophys. Res. Lett.*, **31**, L08306, https://doi.org/10.1029/2003GL019334.

——, S. Levitus, J. Antonov, and S. A. Malmberg, 1998: "Great Salinity Anomalies" in the North Atlantic. *Prog. Oceanogr.*, **41** (1), 1–68, https://doi.org/10.1016/S0079-6611(98)00015-9.

Biló, T. C., F. Straneo, J. Holte, and I. A.-A. Le Bras, 2022: Arrival of new great salinity anomaly weakens convection in the Irminger Sea. *Geophys. Res. Lett.*, **49**, e2022GL098857, https://doi.org/10.1029/2022GL098857.

Brambilla, E., L. D. Talley, and P. E. Robbins, 2008: Subpolar mode water in the northeastern Atlantic: 2. Origin and transformation. *J. Geophys. Res.*, **113**, C04026, https://doi.org/10.1029/2006JC004063.

Caesar, L., G. D. McCarthy, D. J. R. Thornalley, N. Cahill, and S. Rahmstorf, 2021: Current Atlantic meridional overturning circulation weakest in last millennium. *Nat. Geosci.*, **14**, 118–120, https://doi.org/10.1038/s41561-021-00699-z.

Carton, J. A., G. A. Chepurin, J. Reagan, and S. Hkkinen, 2011: Interannual to decadal variability of Atlantic water in the Nordic and adjacent seas. *J. Geophys. Res.*, **116**, C11035, https://doi.org/10.1029/2011JC007102.

Collins, M., and B. Sinha, 2003: Predictability of decadal variations in the thermohaline circulation and climate. *Geophys. Res. Lett.*, **30**, 1306, https://doi.org/10.1029/2002GL016504.

Daniault, N., and Coauthors, 2016: The northern North Atlantic Ocean mean circulation in the early 21st century. *Prog. Oceanogr.*, **146**, 142–158, https://doi.org/10.1016/j.pocean.2016.06.007.

de Boisséson, E., V. Thierry, H. Mercier, G. Caniaux, and D. Desbruyères, 2012: Origin, formation and variability of the subpolar mode water located over the Reykjanes Ridge. *J. Geophys. Res.*, **117**, C12005, https://doi.org/10.1029/2011JC007519.

Desbruyères, D., H. Mercier, and V. Thierry, 2015: On the mechanisms behind decadal heat content changes in the eastern subpolar gyre. *Prog. Oceanogr.*, **132**, 262–272, https://doi.org/10.1016/j.pocean.2014.02.005.

Desbruyères, D. G., H. Mercier, G. Maze, and N. Daniault, 2019: Surface predictor of overturning circulation and heat content change in the subpolar North Atlantic. *Ocean Sci.*, **15**, 809–817, https://doi.org/10.5194/os-15-809-2019.

Fossheim, M., R. Primicerio, E. Johannesen, R. B. Ingvaldsen, M. M. Aschan, and A. V. Dolgov, 2015: Recent warming leads to a rapid borealization of fish communities in the Arctic. *Nat. Climate Change*, **5**, 673–677, https://doi.org/10.1038/nclimate2647.

Foukal, N. P., and M. S. Lozier, 2018: Examining the origins of ocean heat content variability in the eastern North Atlantic subpolar gyre. *Geophys. Res. Lett.*, **45**, 11 275–11 283, https://doi.org/10.1029/2018GL079122.

Fransner, F., A. Olsen, M. Årthun, F. Counillon, J. Tjiputra, A. Samuelsen, and N. Keenlyside, 2023: Phytoplankton abundance in the Barents Sea is predictable up to five years in advance. *Commun. Earth Environ.*, **4**, 141, https://doi.org/10.1038/s43247-023-00791-9.

Fraser, N. J., and S. A. Cunningham, 2021: 120 years of AMOC variability reconstructed from observations using the Bernoulli inverse. *Geophys. Res. Lett.*, **48**, e2021GL093893, https://doi.org/10.1029/2021GL093893.

Fu, Y., L. Feili, J. Karstensen, and C. Wang, 2020: A stable Atlantic meridional overturning circulation in a changing North Atlantic Ocean since the 1990s. *Sci. Adv.*, **6**, eabc7836, https://doi.org/10.1126/sciadv.abc7836.

Furevik, T., 2000: On anomalous sea surface temperatures in the Nordic Seas. *J. Climate*, **13**, 1044–1053, https://doi.org/10.1175/1520-0442(2000)013<1044:OASSTI>2.0.CO;2.

——, 2001: Annual and interannual variability of Atlantic water temperatures in the Norwegian and Barents Seas: 1980–1996. *Deep-Sea Res. I*, **48**, 383–404, https://doi.org/10.1016/S0967-0637(00)00050-9.

Good, S. A., M. J. Martin, and N. A. Rayner, 2013: EN4: Quality controlled ocean temperature and salinity profiles and monthly objective analyses with uncertainty estimates. *J. Geophys. Res. Oceans*, **118**, 6704–6716, https://doi.org/10.1002/2013JC009067.

Grist, J. P., S. A. Josey, Z. L. Jacobs, R. Marsh, B. Sinha, and E. Van Sebille, 2016: Extreme air–sea interaction over the North Atlantic subpolar gyre during the winter of 2013–2014 and its sub-surface legacy. *Climate Dyn.*, **46**, 4027–4045, https://doi.org/10.1007/s00382-015-2819-3.

Hersbach, H., and Coauthors, 2020: The ERA5 global reanalysis. *Quart. J. Roy. Meteor. Soc.*, **146**, 1999–2049, https://doi.org/10.1002/qj.3803.

Holliday, N. P., and Coauthors, 2008: Reversal of the 1960s to 1990s freshening trend in the northeast North Atlantic and Nordic Seas. *Geophys. Res. Lett.*, **35**, L03614, https://doi.org/10.1029/2007GL032675.

——, and Coauthors, 2020: Ocean circulation causes the largest freshening event for 120 years in eastern subpolar North Atlantic. *Nat. Commun.*, **11**, 585, https://doi.org/10.1038/s41467-020-14474-y.

Horel, J., 1984: Complex principal component analysis: Theory and examples. *J. Climate Appl. Meteor.*, **23**, 1660–1673, https://doi.org/10.1175/1520-0450(1984)023<1660:CPCATA>2.0.CO;2.

Hughes, S. L., N. P. Holliday, E. Colbourne, V. Ozhigin, H. Valdimarsson, S. Østerhus, and K. Wiltshire, 2009: Comparison of in situ time-series of temperature with gridded sea surface temperature datasets in the North Atlantic. *ICES J. Mar. Sci.*, **66**, 1467–1479, https://doi.org/10.1093/icesjms/fsp041.

IOC, SCOR, and IAPSO, 2010: The International Thermodynamic Equation of Seawater—2010: Calculation and use of thermodynamic properties. Intergovernmental Oceanographic Commission, Manuals and Guides 56, 220 pp., https://teos-10.org/pubs/TEOS-10_Manual.pdf.

Ishii, M., A. Shouji, S. Sugimoto, and T. Matsumoto, 2005: Objective analyses of sea-surface temperature and marine meteorological variables for the 20th century using ICOADS and the Kobe Collection. *Int. J. Climatol.*, **25**, 865–879, https://doi.org/10.1002/joc.1169.

Jacob, D., H. Goettel, J. Jungclaus, M. Muskulus, R. Podzun, and J. Marotzke, 2005: Slowdown of the thermohaline circulation causes enhanced maritime climate influence and snow cover over Europe. *Geophys. Res. Lett.*, **32**, L21711, https://doi.org/10.1029/2005GL023286.

Jones, S. C., N. J. Fraser, S. A. Cunningham, A. D. Fox, and M. E. Inall, 2023: Observation-based estimates of volume, heat, and freshwater exchanges between the subpolar North Atlantic interior, its boundary currents, and the atmosphere. *Ocean Sci.*, **19**, 169–192, https://doi.org/10.5194/os-19-169-2023.

Josey, S. A., J. J. Hirschi, B. Sinha, A. Duchez, J. P. Grist, and R. Marsh, 2018: The recent Atlantic cold anomaly: Causes, consequences, and related phenomena. *Annu. Rev. Mar. Sci.*, **10**, 475–501, https://doi.org/10.1146/annurev-marine-121916-063102.

Koman, G., W. E. Johns, A. Houk, L. Houpert, and F. Li, 2022: Circulation and overturning in the eastern North Atlantic subpolar gyre. *Prog. Oceanogr.*, **208**, 102884, https://doi.org/10.1016/j.pocean.2022.102884.

Krahmann, G., M. Visbeck, and G. Reverdin, 2001: Formation and propagation of temperature anomalies along the North Atlantic Current. *J. Phys. Oceanogr.*, **31**, 1287–1303, https://doi.org/10.1175/1520-0485(2001)031<1287:FAPOTA>2.0.CO;2.

Langehaug, H. R., A. B. Sandø, M. Årthun, and M. Ilicak, 2018: Variability along the Atlantic water pathway in the forced Norwegian Earth System Model. *Climate Dyn.*, **52**, 1211–1230, https://doi.org/10.1007/s00382-018-4184-5.

Li, F., and Coauthors, 2021: Subpolar North Atlantic western boundary density anomalies and the meridional overturning. *Nat. Commun.*, **12**, 3002, https://doi.org/10.1038/s41467-021-23350-2.

Lozier, M. S., and Coauthors, 2017: Overturning in the Subpolar North Atlantic Program: A new international ocean observing system. *Bull. Amer. Meteor. Soc.*, **98**, 737–752, https://doi.org/10.1175/BAMS-D-16-0057.1.

——, and Coauthors, 2019: A sea change in our view of overturning in the subpolar North Atlantic. *Science*, **363**, 516–521, https://doi.org/10.1126/science.aau6592.

Marsh, R., 2000: Recent variability of the North Atlantic thermohaline circulation inferred from surface heat and freshwater fluxes. *J. Climate*, **13**, 3239–3260, https://doi.org/10.1175/1520-0442(2000)013<3239:RVOTNA>2.0.CO;2.

McCarthy, G. D., and L. Caesar, 2023: Can we trust projections of AMOC weakening based on climate models that cannot reproduce the past? *Philos. Trans. Roy. Soc.*, **A381**, 20220193, https://doi.org/10.1098/rsta.2022.0193.

McDougall, T. J., and P. M. Barker, 2011: Getting started with TEOS-10 and the Gibbs Seawater (GSW) oceanographic toolbox. Tech. Rep. SCOR/IAPSO WG127, 34 pp., https://www.teos-10.org/pubs/Getting_Started.pdf.

Merryfield, W. J., and Coauthors, 2020: Current and emerging developments in subseasonal to decadal prediction. *Bull. Amer. Meteor. Soc.*, **101**, E869–E896, https://doi.org/10.1175/BAMS-D-19-0037.1.

O'Mahony, M., 1986: *Sensory Evaluation of Food: Statistical Methods and Procedures.* 1st ed. Routledge, 510 pp.

Onarheim, I. H., T. Eldevik, M. Årthun, R. B. Ingvaldsen, and L. H. Smedsrud, 2015: Skillful prediction of Barents Sea ice

cover. *Geophys. Res. Lett.*, **42**, 5364–5371, https://doi.org/10.1002/2015GL064359.

Passos, L., H. R. Langehaug, M. Årthun, T. Eldevik, I. Bethke, and M. Kimmritz, 2023: Impact of initialization methods on the predictive skill in NorCPM: An Arctic–Atlantic case study. *Climate Dyn.*, **60**, 2061–2080, https://doi.org/10.1007/s00382-022-06437-4.

Payne, M. R., G. Danabasoglu, N. Keenlyside, D. Matei, A. K. Miesner, S. Yang, and S. G. Yeager, 2022: Skilful decadal-scale prediction of fish habitat and distribution shifts. *Nat. Commun.*, **13**, 2660, https://doi.org/10.1038/s41467-022-30280-0.

Petit, T., M. S. Lozier, S. A. Josey, and S. A. Cunningham, 2020: Atlantic deep water formation occurs primarily in the Iceland Basin and Irminger Sea by local buoyancy forcing. *Geophys. Res. Lett.*, **47**, e2020GL091028, https://doi.org/10.1029/2020GL091028.

——, ——, ——, and ——, 2021: Role of air–sea fluxes and ocean surface density in the production of deep waters in the eastern subpolar gyre of the North Atlantic. *Ocean Sci.*, **17**, 1353–1365, https://doi.org/10.5194/os-17-1353-2021.

Piecuch, C. G., R. M. Ponte, C. M. Little, M. W. Buckley, and I. Fukumori, 2017: Mechanisms underlying recent decadal changes in subpolar North Atlantic Ocean heat content. *J. Geophys. Res. Oceans*, **122**, 7181–7197, https://doi.org/10.1002/2017JC012845.

Rayner, N. A., D. E. Parker, E. B. Horton, C. K. Folland, L. V. Alexander, D. P. Rowell, E. C. Kent, and A. Kaplan, 2003: Global analyses of sea surface temperature, sea ice, and night marine air temperature since the late nineteenth century. *J. Geophys. Res.*, **108**, 4407, https://doi.org/10.1029/2002JD002670.

Robson, J. I., R. T. Sutton, and D. M. Smith, 2012: Initialized decadal predictions of the rapid warming of the North Atlantic Ocean in the mid 1990s. *Geophys. Res. Lett.*, **39**, L19713, https://doi.org/10.1029/2012GL053370.

Saravanan, R., and J. C. Mcwilliams, 1998: Advective ocean–atmosphere interaction: An analytical stochastic model with implications for decadal variability. *J. Climate*, **11**, 165–188, https://doi.org/10.1175/1520-0442(1998)011<0165:AOAIAA>2.0.CO;2.

Sherwin, T. J., M. O. Williams, W. R. Turrell, S. L. Hughes, and P. I. Miller, 2006: A description and analysis of mesoscale variability in the Färoe-Shetland Channel. *J. Geophys. Res.*, **111**, C03003, https://doi.org/10.1029/2005JC002867.

Speer, K., and E. Tziperman, 1992: Rates of water mass formation in the North Atlantic Ocean. *J. Phys. Oceanogr.*, **22**, 93–104, https://doi.org/10.1175/1520-0485(1992)022%3C0093:ROWMFI%3E2.0.CO;2.

Thierry, V., E. de Boisséon, and H. Mercier, 2008: Interannual variability of the subpolar mode water properties over the Reykjanes Ridge during 1990–2006. *J. Geophys. Res.*, **113**, C04016, https://doi.org/10.1029/2007JC004443.

Walin, G., 1982: On the relation between sea-surface heat flow and thermal circulation in the ocean. *Tellus*, **34A**, 187–195, https://doi.org/10.3402/tellusa.v34i2.10801.

Watanabe, M., and M. Kimoto, 2000: On the persistence of decadal SST anomalies in the North Atlantic. *J. Climate*, **13**, 3017–3028, https://doi.org/10.1175/1520-0442(2000)013%3C3017:OTPODS%3E2.0.CO;2.

Yashayaev, I., and D. Seidov, 2015: The role of the Atlantic water in multidecadal ocean variability in the Nordic and Barents Seas. *Prog. Oceanogr.*, **132**, 68–127, https://doi.org/10.1016/j.pocean.2014.11.009.

Yeager, S. G., A. R. Karspeck, and G. Danabasoglu, 2015: Predicted slowdown in the rate of Atlantic sea ice loss. *Geophys. Res. Lett.*, **42**, 10 704–10 713, https://doi.org/10.1002/2015GL065364.

Yin, J., and M. Zhao, 2021: Influence of the Atlantic meridional overturning circulation on the U.S. extreme cold weather. *Commun. Earth Environ.*, **2**, 218, https://doi.org/10.1038/s43247-021-00290-9.

Zhao, J., A. Bower, J. Yang, X. Lin, and N. P. Holliday, 2018: Meridional heat transport variability induced by mesoscale processes in the subpolar North Atlantic. *Nat. Commun.*, **9**, 1124, https://doi.org/10.1038/s41467-018-03134-x.